Composite Nanoarchitectonics with Polythiophene, MWCNTs-G, CuO and Chitosan as a Voltammetric Sensor for Detection of Cd(II) Ions
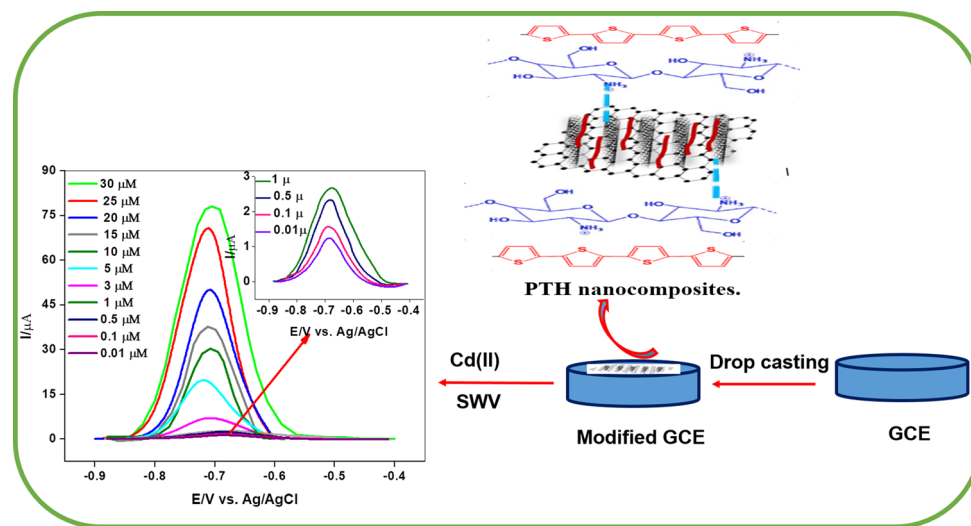
Hanaa H. AL-Refai[1,2] · Aisha A. Ganash[1] · Mahmoud A. Hussein[1,3]

Abstract

In this study, we describe an electrochemical method for detecting Cd(II) ions, utilizing a glassy carbon electrode (GCE) modified with polythiophene (PTH)/multi-walled carbon nanotubes with grapheme (MECNTs-G), chitosan (CS), and CuO. The PTH/MWCNTs-G/CS/CuO was prepared via an in situ oxidative polymerization route. XRD and FT-TR analysis confirmed that the nanocomposites were successfully prepared. TEM, SEM, EDX, TGA, and DTG were utilized to study the morphological and thermal properties of the newly synthesized materials. The electrochemical detection of Cd(II) was achieved by CV and SWV. The cadmium ions exhibited a linear relationship at concentrations of 30–0.01 μM with the PTH/MWCNTs-G/CS/CuO/GCE. The limit of detection and limit of quantification were found to be 0.014 and 0.049 μM, respectively. The stability, selectivity, and reproducibility of the modified electrode were also studied. Good recovery was achieved for the practical application of PTH/MWCNTs-G/CS/CuO/GCE in a tap-water sample.

Graphic Abstract

✉ Hanaa H. AL-Refai
HALREFAI0017@stu.kau.edu.sa;
HHJUHANI@taibahu.edu.sa

Aisha A. Ganash
aganash@kau.edu.sa

Mahmoud A. Hussein
mahussein74@yahoo.com; maabdo@kau.edu.sa

[1] Chemistry Department, Faculty of Science, King Abdulaziz University, P.O. Box 80203, Jeddah 21589, Saudi Arabia

[2] Chemistry Department, Faculty of Science, Taibah University, Yanbu 46421, Saudi Arabia

[3] Polymer Chemistry Lab., Chemistry Department, Faculty of Science, Assiut University, Assiut 71516, Egypt

1 Introduction

Due to the development of industry, the contamination of groundwater by heavy metals is an important issue in several regions around the world. These pollutants can accumulate in certain locations and are detrimental to both the environment and human health. The World Health Organization (WHO) set the acceptable threshold limit of cadmium at 3 ppb (0.024 μM) in drinking water [1]. Therefore, it is necessary to have a method to rapidly detect this contaminant with sufficient sensitivity. Diverse techniques with high performance, such as inductively coupled plasma mass spectrometry (ICP-MS) [2, 3] and high performance liquid chromatography (HPLC) [4, 5], have been developed to detect Cd(II). However, these techniques have some drawbacks including the need for expensive apparatus and that procedures are time-consuming. Conversely, voltammetric techniques, such as cyclic voltammetry (CV), differential pulse voltammetry (DPV), and square wave voltammetry (SWV) have been utilized for Cd(II) detection and have the benefits of requiring cost-effective apparatus, only simple handling, on-site detection, and superior sensitivity [6]. Conventionally, bulk electrodes still have some issues in voltammetric measurement such as high oxidation potential and possible interference from any ions present in samples such as Fe(II), Fe(III), Cu(II), Zn(II), Na + and Pb(II). However, modifications of the electrode can overcome these issues and modified electrodes exhibit superior sensitivity and high performance. Studies have reported on Cd(II) ions detection in an aqueous solution; for example, Zheng et al. [7] prepared mesoporous ɤ-alumina (M-ɤ-Al$_2$O$_3$) and modified it into a carbon paste using DPV. The designed electrode displayed a dynamic range of 0.01–10 μM with limits of detection (LOD) of 2 nM. Göde et al. [8] used calixarene and reduce graphene oxide CA/RGO/GCE. The modified electrode displayed an LOD of 2×10^{-11} M using SWV. It was reported by Wu et al. [9] that the modified GCE with Fe$_3$O$_4$ and functionalized MWCNT achieved more efficient Cd(II) detection. The nanocomposite (NCs) was prepared using the hydrothermal procedure and showed a high response with LOD of 0.014 μM. Sengupta et al. [1] designed an electrode for Cd(II) detection by incorporating an iron-aluminate mixed metal oxide and chitosan on GCE via a solid-phase procedure. CS-MMON/GCE was utilized to determine the Cd(II) by DPV with an LOD of 0.068 ppt. More recently, Moutcine et al. [10] used ZnO nanoparticles as modified materials via the SWV technique in drinking water with an LOD of 4.2 nM. In the case of using the conducting polymers (CP) in modification potential, Dai et al. [11] reported that polypyrrole/graphene oxide PPy/GO was fabricated by an in situ oxidative polymerization.

The fabricated electrode showed high conductivity with a wide dynamic range (5–150 μg L^{-1}). Non-destroyable surface functionalization of MWCNTs can be achieved with chitosan without having an effect on the electronic and mechanical properties of the nanomaterials [12]. Chitosan is a random copolymer that possesses unique properties including great potential for modifications to improve desired properties of non-toxicity, and biodegradability [13, 14]. In addition, CuO is an interesting material due to its low cost and catalysis [15]. The combination of CuO, MWCNTs, G, and CS in a CP, such as the polythiophene (PTH) matrix, is an attractive way to create modified working electrodes. MWCNTs-G/CS/CuO supports the diffusion of ions to the electrode surface by increasing the active sites where the PTH assist to accelerate the electrode kinetic. However, there are limited reports on using the PTH/MWCNTs-G/CS/CuO/GCE as a voltammetric sensor for the detection of Cd(II) ions. Therefore, the main aim of this work was to synthesize a series of nanocomposites based on PTH, PTH/MWCNTs-G, PTH/MWCNTs-G/CS, and PTH/MWCNTs-G/CS/CuO. This is a continuation of our previous research, which aimed to fabricate sensors for pollutants detection [16–22]. The nanocomposites were synthesized via an in situ oxidative polymerization route and characterized using different techniques including FT-IR, XRD, SEM, EDX, TEM, TGA, and DTG. The fabricated materials were applied to modify GCE for the detection of Cd(II) using CV and SWV and the stability, reproducibility, selectivity, and recovery were also studied.

2 Experimental Design

2.1 Chemicals and Reagents

Thiophene was used as purchased from PDH (England). MWCNTs (short) (diameter = 5–15 nm, L = 0.5–2 μm), G (diameter = 5–10um, thickness = 3–10 nm, purity > 99.5%), and CuO nano-chains (diameter = 35–42 nm, L = 1.0–1.6 μm, purity = 99%) were obtained from XFNANO Inc. (China). Chitosan (medium MW) was obtained from Sisco Research Laboratories Pvt. Ltd (India). Chloroform (99.8%), ferric chloride anhydrous (98%) (FeCl3), and methanol (99.8%) were sourced from Acros Organic. Acetone (99.5%) was purchased from Panreac Quimica. Diamond paper and aluminum oxide (AO) paper were obtained from Bio-Logic Science Instruments, France. CdCl$_2$.2H$_2$O were procured from Techno Pharma Chem. All solutions were prepared using double distilled water (DDW).

2.2 Instrumentation

AJEOL JSM-7610F scanning electron microscopy (FE-SEM) and energy dispersive X-ray analysis (EDX) were used to study the surface condition. The combination between the nanomaterials was confirmed using a JEOL JEM 1400 and transmission electron microscopy (TEM). A Rigaku D/max 2550 VB/PC was used for X-ray diffraction (XRD) analysis and Spotlight 400 FT-IR was used for fourier transform-infrared spectra (FT-IR) analysis. Thermogravimetric analysis was carried out using a NETZSCH (Germany) with a standard heating procedure from 20 to 100 °C and held at 100 °C for 20 min in N_2, after which the gas changed to air and temperature was increased to 900 °C.

Electrochemical measurements were obtained using a SP-200 potentiostat/galvanostat instrument from Biologic equipped with EC-Lab software for data analysis. The working electrode (W.E) was made of GCE and platinum rod was used as the counter electrode (A.E), while the reference electrode (R.E) was Ag/AgCl (3 M KCl). Voltammetric studies were carried out in solution containing 2 mM $[Fe(CN)_6]^{3-/4-}$ in 0.1 M KCl redox. The applied potentials for CVs were from – 0.2 to 0.8 V at a scan rate (v) of 0.05 Vs^{-1} against RE. For Electrochemical Impedance Spectrometric (EIS), the potential was set at 0.235 V against RE, with frequency ranging from 1 Hz to 100 kHz. Electrochemical detection of Cd(II) was achieved by SWV from – 0.9 to – 0.6 V, with a pulse height (P_H) of 0.05 V and width (P_W) of 0.05×10^{-3} s, and as step height (S_H) of 0.02 V.
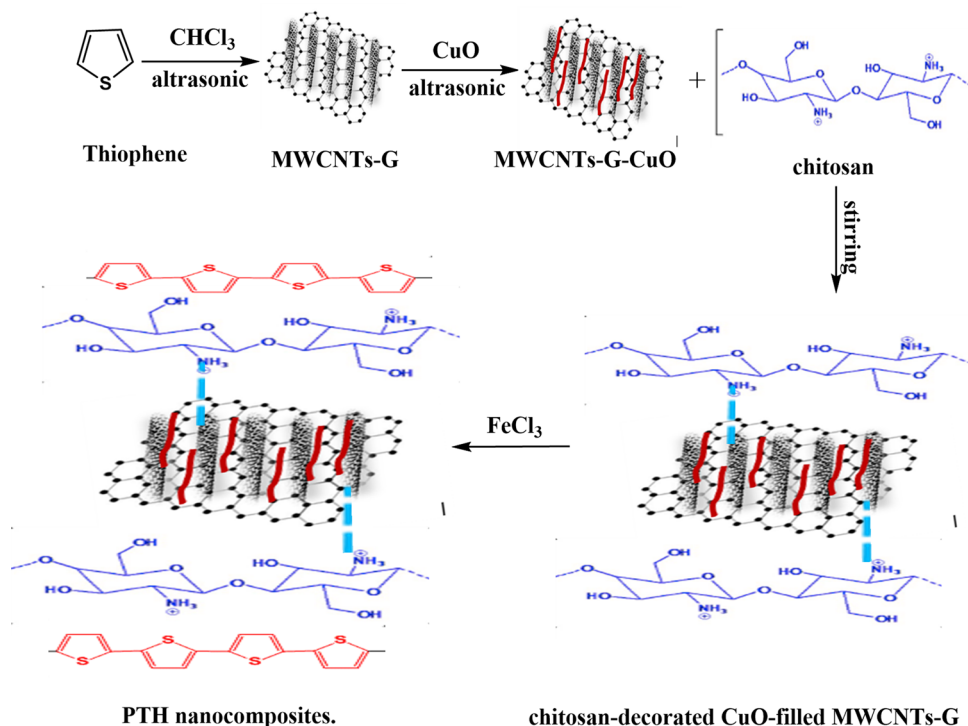
2.3 Preparation of MWCNTs-G NCs

MWCNTs-G NCs were prepared by blending MWCNTs and graphene at a 1:1 ratio [23]. We mixed 100 mg of G with 5 mL of DDW and used sonication for 2 h in an ultrasonic bath. The MWCNTs (100 mg) were dispersed in 5 mL DDW and underwent sonication for 2 h. G and MWCNTs were blended by sonication for 2 h. The black powder product was filtered and washed with DDW and dried at 70 °C.

2.4 Preparation of PTH and PTH/MWCNTs-G

The NCs were synthesized by an in situ chemical oxidative polymerization as depicted in [24, 25] with minor changes. A solution of 11.88 mmol (95% weight) of thiophene and 50 mL of chloroform was sonicated for 30 min to create a homogeneous suspension. Thereafter, 0.05 g of MWCNTs was included in the above mixture, which was then sonicated for 45 min. Then, a solution containing 8.2 g (50 mmol) of $FeCl_3$ in 100 mL chloroform was added to thiophene/MWCNTs-G and mixed by continuous stirring for 24 h. The NCs were filtered and washed with methanol, DDW and acetone until the filtrate was colorless. During this procedure, it was noticed that the color of NCs changed from black to brown. Finally, the product was dried at 70 °C. The pure polymer was also

Fig. 1 Schematic of the formation of PTH/MWCNTs-G/CS/CuO

synthesized without including MWCNTs-G by utilizing the same procedure.

2.5 Preparation of PTH/MWCNTs-G/CS/CuO

The NCs were prepared as depicted in [23, 26] with minor changes (Fig. 1). A solution containing 11.25 mmol (90% weight) of thiophene and 50 mL of chloroform was sonicated for 30 min. Thereafter, 0.05 g of MWCNTs-G was added to the mixture and sonicated for 45 min. Following this, 0.05 g CuO nanochain was added to PTH/MWCNTs-G, which was then sonicated for 30 min. A solution containing 0.5 g chitosan in 4% CH_3COOH was then added into PTH/MWCNTs-G/CuO by constant stirring for 1 h. Then an $FeCl_3$ suspension was added to the mixture with constant stirring for 24 h. The resulting NCs were then filtered and washed using methanol, followed by DDW and acetone. The synthesized polymer solution was then cast onto petri dishes, and the solvent was allowed to evaporate for 24 h to obtain a film polymer. The same procedure was used to prepare PTH/MWCNTs-G/CS but without adding CuO.

2.6 Modification of the Electrode

The GCE was carefully cleaned with diamond and aluminum paper and was then rinsed with DDW. The GCE was then sonicated in DDW followed by ethanol for 2 min. A thin layer was prepared by drop casting the synthesized polymer on the surface of GCE; then, the modified electrode was allowed to dry at room temperature.

3 Results and Discussion

3.1 Characterization of Nanocomposites

The XRD patterns obtained for PTH, MWCNTs-G, PTH/MWCNTs-G, PTH/MWCNTs-G/CS, and PTH/MWCNTs-G/CS/CuO are shown in Fig. 2. With regard to the PTH (Fig. 2a), the broad peak at 2θ (14°–30°) elucidates its amorphous structure. The peak around 2θ (22°) is associated with the π–π stacking nature of PTH [15, 27–29]. The pattern of MWCNTs-G (Fig. 2b) exhibited a well-defined peak around 2θ (26.6°) that was related to the (0 0 2) diffraction plane of MWCNTs [30]. A low-intensity peak at 2θ (23°) was due to amorphous carbon and a low-intensity broad peak around 2θ (43°) could be attributed to the hexagonal graphite nature [21]. As can be seen in Fig. 2c, there was no noticeable difference in either peak position or shape of MWCNTs-G, and only a minor reduction in the peak intensity of NCs, indicating the formation of MWCNTs-G with a polythiophene matrix. The XRD pattern of PTH/MWCNTs-G/CS (Fig. 2d) shows characteristic peaks of PTH and MWCNTs,
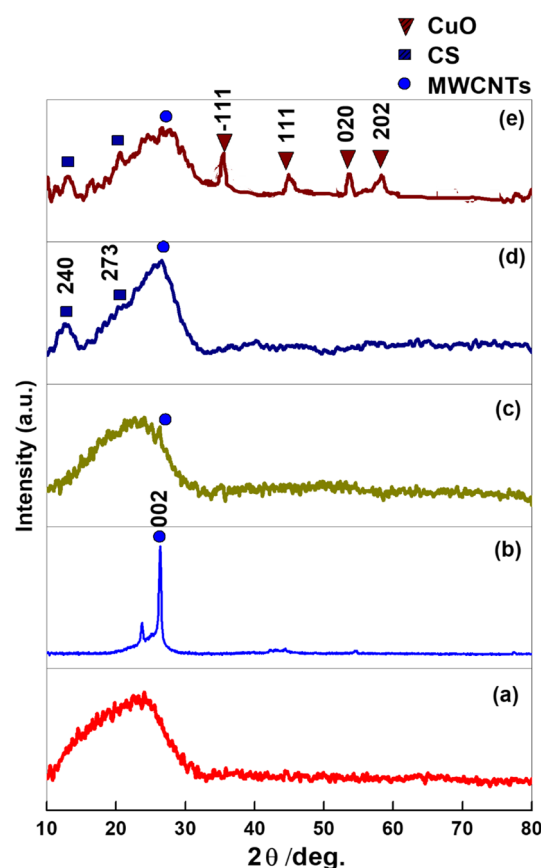

Fig. 2 XRD patterns of (a) PTH, (b) MWCNTs-G, (c) PTH/MWCNTs-G, (d) PTH/MWCNTs-G/CS, and (e) PTHMWCNTs-G/CS/CuO

while the peaks at 2θ (20.2°) and 2θ (12.0°) corresponding to (2 7 3) and (2 4 0) respectively, are related to chitosan [31]. In the case of PTH/MWCNTs-G/CS/CuO (Fig. 2e), all characteristic peaks of PTH, MWCNTs-G, and CS appear in the XRD pattern. Besides, small peaks observed at 2θ (35°, 38.8°, 53°, and 58.5°) corresponded with ($\bar{1}$11), (1 1 1), (020), and (2 0 2), and were well indexed with JCPDS No. 45–0937 (Figure S1). These results suggest the presence of a crystalline CuO nanochain in PTH/MWCNTs-G/CS/CuO.

FT-IR spectra were studied to investigate the chemical structures and functional groups of the NCs. Figure 3 shows the FT-IR spectra for pure PTH, MWCNTs-G, PTH/MWCNTs-G, PTH/MWCNTs-G/CS, and PTH/MWCNTs-G/CS/CuO. For pure PTH, a well-defined peak appears in the fingerprint region at 788 cm^{-1} and was related to C-H out of plane vibration in the 2,5- substitution (α–α$^-$ coupling) polymer ring formed during polymerization, while the band at 620 cm^{-1} corresponds to C-S bending, indicating the presence of thiophene [32, 33]. The band located at 1042 cm^{-1} indicates C-H in plane deformation. Furthermore, the peak appearance at 1340 cm^{-1} is due to the C=C stretch of the quinoid ring. The appearance of a band at 1440 cm^{-1} and
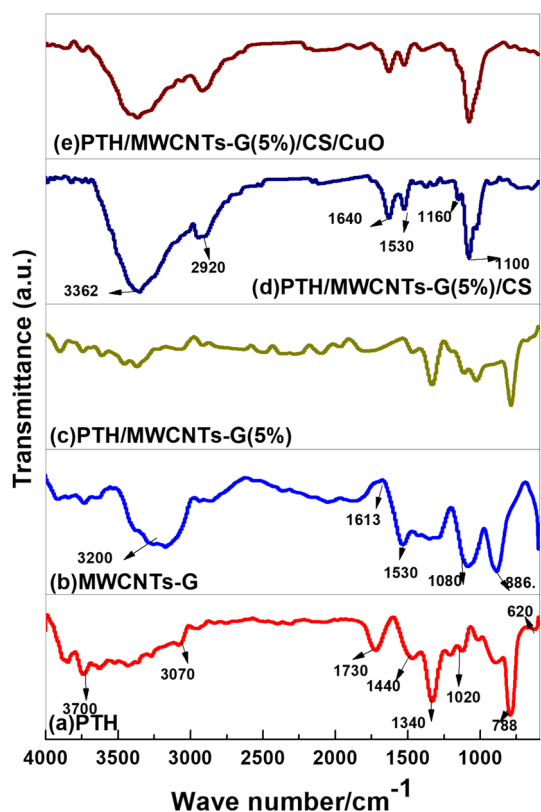
Fig. 3 FT-IR spectra of (a) PTH, (b) MWCNTs-G, (c) PTH/MWCNTs-G, (d) PTH/MWCNTs-G/CS, and (e) PTHMWCNTs-G/CS/CuO

1730 cm^{-1} corresponds to C=C symmetric and aromatic C=C (benzenoid) stretching vibrations, respectively [15, 30, 34]. The broadband located at 3070–3700 cm^{-1} may be attributed to a C–H symmetric aromatic stretching band [35].

In the FT-IR spectrum for the MWCNTs-G (Fig. 3b), the band at 886 cm^{-1} corresponds to aromatic C–H bending and the band located at 1080 cm^{-1} indicates C–O bending. The existence of these functional groups in the MWCNTs shows that they were introduced during manufacturing [36]. The band at 1530 cm^{-1} is related to plane vibration C–C of graphitic walls of MWCNTs, while the band at 1613 cm^{-1} can be attributed to the C=C stretching mode of MWCNTs. The broad peak located around 3200 cm^{-1} suggests the presence of O–H stretching of the moisture content [30, 37]. All the peaks attributed to MWCNTs-G and PTH appear in Fig. 3c, suggesting the formation of PTH/MWCNTs-G NCs. However, compared to a pure polymer, the peak related to benzenoid (1730 cm^{-1}) disappeared, while the peak related to the quinoid structure (1340 cm^{-1}) became strong. The increasing quinoid assisted in reducing the forbidden gap and resulted in higher electrical conductivity of the hybrid materials [32]. In the case of PTH/MWCNTs-G/CS, Fig. 3d shows the characteristic peaks of chitosan. A small peak

around 1530 cm^{-1} is related to the N–H bending of secondary amide, and the peak at 1640 cm^{-1} is the amide stretch C=O after PTH conjugation [38]. The characteristic bands that appear at 1100 cm^{-1} and 1160 cm^{-1} show the presence of a C–O–C bridge. The peak at 2920 cm^{-1} is related to a C-H stretching vibration, while the band located around 3362–3282 cm^{-1} is related to the stretching vibration modes of NH and OH [26, 34]. The characteristic peaks of PTH/MWCNTs-G may overlap or become covered during decoration processing. In the case of PTH/MWCNTs-G/CS/CuO (Fig. 3e), the FT-IR spectra were very similar to the previous spectra and the CuO signal was not observed, suggesting that CuO may have been formed inside the MWCNTs. These results are in agreement with TEM and SEM, results for which will be discussed later.

Typical TEM images of the pure polymer and modified polymers are shown in Fig. 4. From the TEM image, Fig. 4a shows the single-layer film-like structure of PTH. Figure 4b shows that MWCNTs were impeded with a homogeneous distribution within the graphene sheet. The TEM image of PTH/MWCNTs-G (Fig. 4c) shows an irregular rod-like morphology, and the MWCNTs-G are covered by the PTH. The preparation method helps the PTH to uniformly coat the surface of the nanocomposite [39]. These results were confirmed from the increased thickness of MWCNT-G by SEM analysis. In Fig. 4d it is clear that MWCNTs-G/CS/CuO was coated by the bulky micron-sized PTH, and the CuO nanochain with a mean diameter around 35 nm was deposited on the wall of MWCNTs.

The SEM image of pure PTH (Fig. 5a) shows an amorphous structure of macromolecular flakes and a crushed paper-like structure that are closely interconnected, which reflected the oxidant (FeCl$_3$) involved during the in situ oxidative polymerization process [40]. Figure 5b displays MWCNTs effectively mixed and embedded in the thin graphene sheet. However, the surface of PTH/MWCNTs-G nanocomposites exhibits a plate-like morphology (Fig. 5c). The reason for this appearance may be the incorporation of MWCNTs-G inside the PTH matrix by π-π conjugated interactions between the polymer and MWCNTs-G during the polymerization process [41]. The CuO nanochain, which consisted of CuO nanoparticles with a diameter of 35–42 nm, displayed a fibrous structure (Fig. 5d). Additionally, the SEM image of the PTH/MWCNTs-G/CS/CuO (Fig. 5e) composite revealed that the MWCNTs-G and CuO were uniformly covered with a layer of PTH film. It can be confirmed from EDX analysis (Fig. 5f) that the NCs were composed of C, N, O, S, and Cu. These results confirm that the PTH/MWCNTs-G/CS/CuO were successfully prepared.

TGA and DTG were used to examine the thermal stability and weight loss of the polymers, and the data are shown in Fig. 6. The decomposition of PTH is very similar to that reported for polythiophene [42–45]. The typical TGA
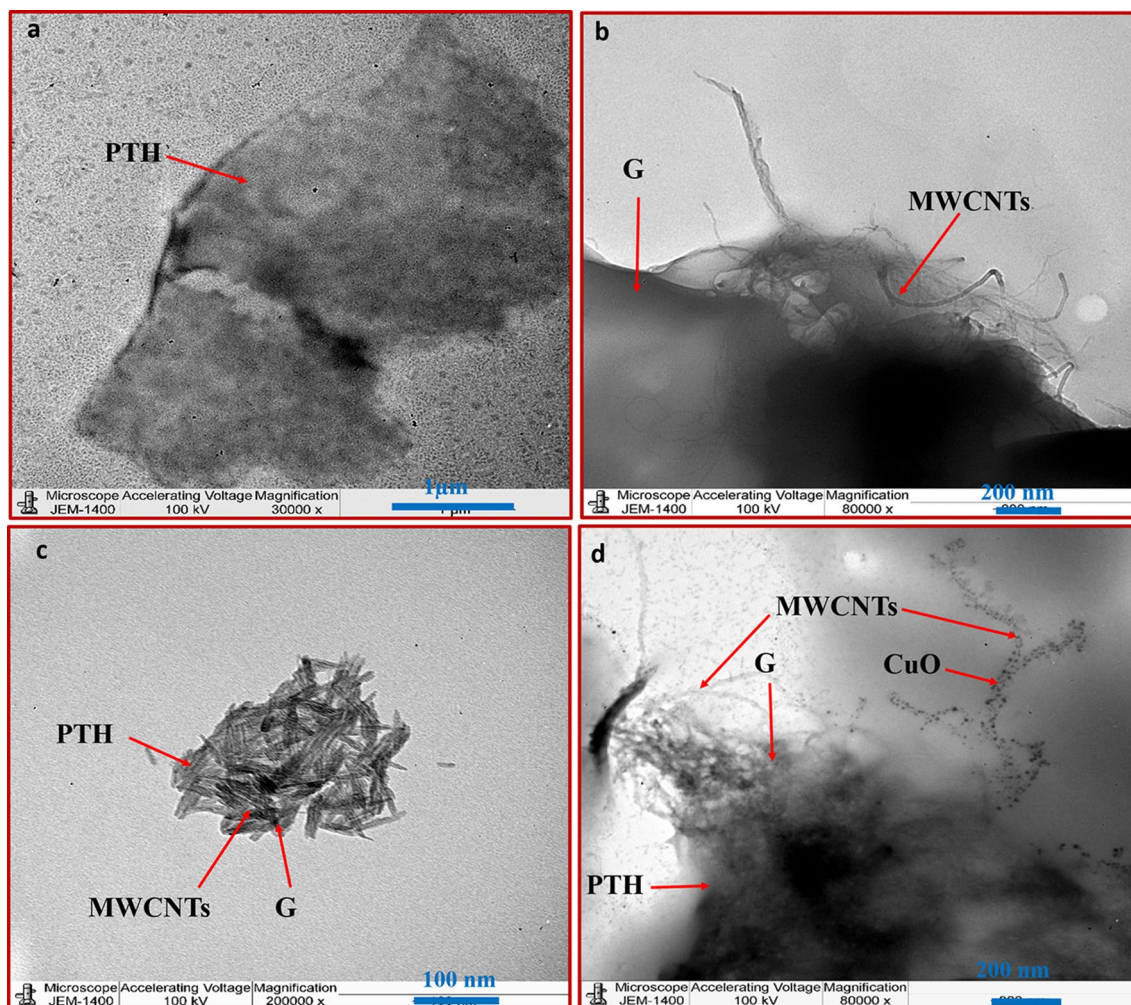
Fig. 4 TEM images of **a** PTH, **b** MWCNTs-G, **c** PTH/MWCNTs-G, and **d** PTH/MWCNTs-G/CS/CuO

curve showed a two-step weight loss, the first due to solvent evaporation, the second occurring between 325 and 480 °C and due to the thermal degradation of PTH. Similar behavior was observed for PTH/MWCNTs-G, suggesting that this nanocomposite shows a similar degradation process. As can be seen in Table 1, the maximum polymer decomposition temperature (PDTmax) and final polymer decomposition temperature (CDT final) obtained from the DTG and TGA curves [19, 46] exhibited higher temperatures for PTH/MWCNTs-G compared to the pure polymer. These results demonstrate the MWCNTs-G effect, which increases the thermal stability of NCs [47]. In the case of the composite film PTH/MWCNTs-G/CS, the first degradation step started between 30 and 120 °C with 25% weight loss, due to the loss of H_2O. The second degradation between 185 and 243 °C included a 50% weight loss, indicating that thermal degradation of chitosan took place [38, 48, 49]. A 90% weight loss occurred between 378

and 418 °C due to the thermal degradation of the polymer chain. The same behavior was observed for the second polymer PTH/ MWCNTs-G/CS/CuO, but only the final degradation step appeared at a higher temperature (446 °C) compared to the polymer without CuO. These results indicate that the thermal stability of the polymer was improved by incorporating CuO into the polymer film. Table 1 shows the results of T_{10}, T_{25}, and T_{50}, which represent thermal degradation at 10%, 25%, and 50% respectively. These values for the PTH/MWCNTs-G were 347, 416, and 443 °C, respectively, demonstrating that the PTH/MWCNTs-G had the highest thermal stability. On the other hand, polymer grafting with chitosan exhibited an earlier and greater weight loss. This difference in behavior can be attributed to the high tendency of chitosan to adsorption of water, which could weaken hydrogen bonding [38, 49, 50]. These results confirm that the incorporation of polythiophene with MWCNTs-G led to an enhancement of the thermal stability of PTH/MWCNTs-G.
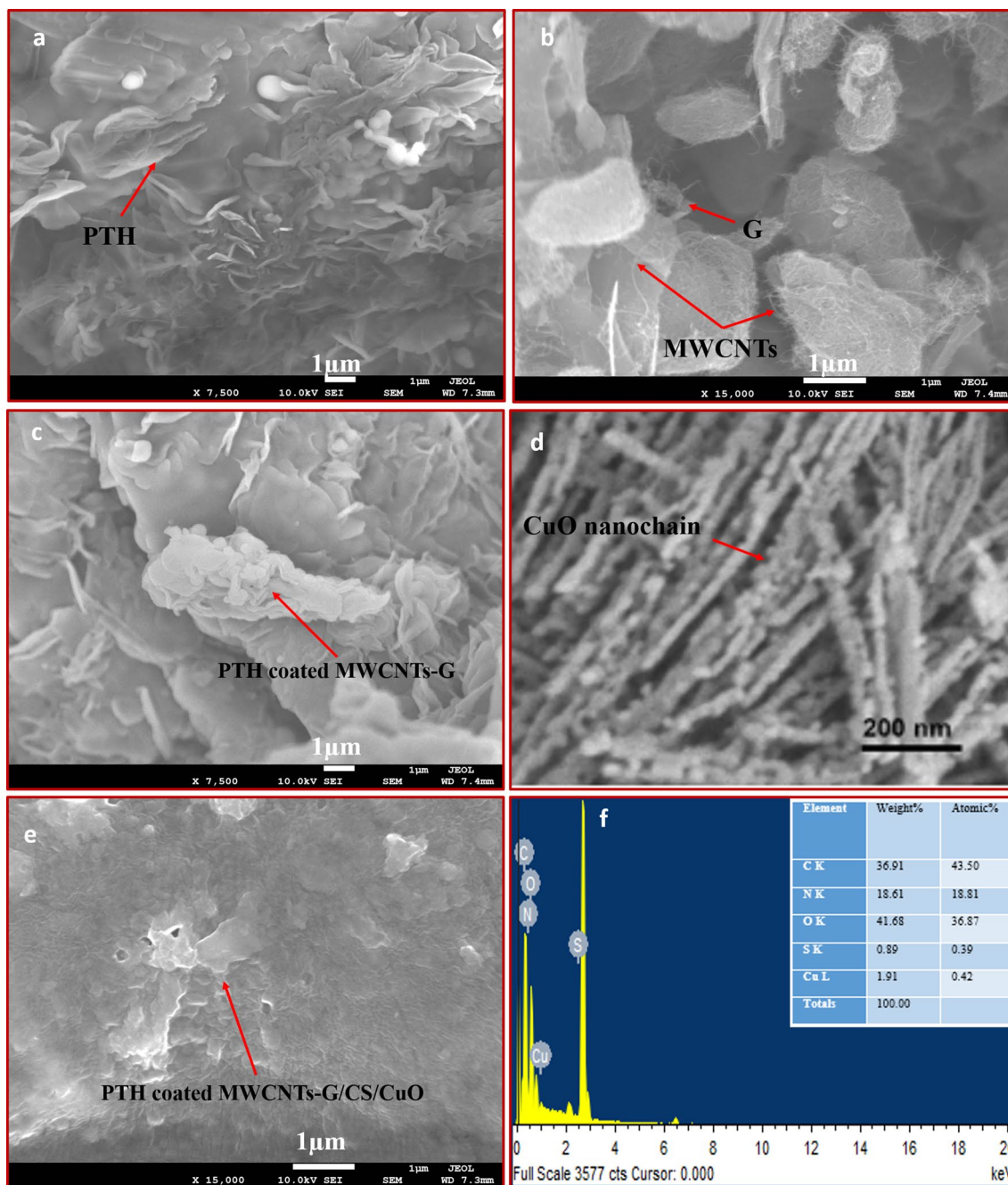
Fig. 5 SEM images of **a** PTH, **b** MWCNTs-G, **c** PTH/MWCNTs-G, **d** CuO, **e** PTH/MWCNTs-G/CS/CuO, and **f** the EDX of PTH/MWCNTs-G/CS/CuO

3.2 Electrochemical Behavior of Different Modified Electrodes

The CVs of different modified electrodes were carried out in 2 mM $[Fe(CN)_6]^{3-/4-}$ and 0.1 M of KCl and the applied potentials were from -0.2 to 0.8 V at a scan rate (v) of 0.05 Vs^{-1} against RE (Fig. 7). It is apparent that PTH/MWCNTs-G/CS/CuO/GCE exhibited a higher current compared to other electrodes. This may be due to the high electrical conductivity of the polymer and the high surface area of the nanomaterial, which provides a large number of adsorption sites, enhancing analyte diffusion at its surface.

The effective surface areas were calculated by CV in the solution containing 2 mM $[Fe(CN)_6]^{3-/4-}$ and 0.1 M KCl using the Randles–Sevcik equation (Eq. 1) [51]:

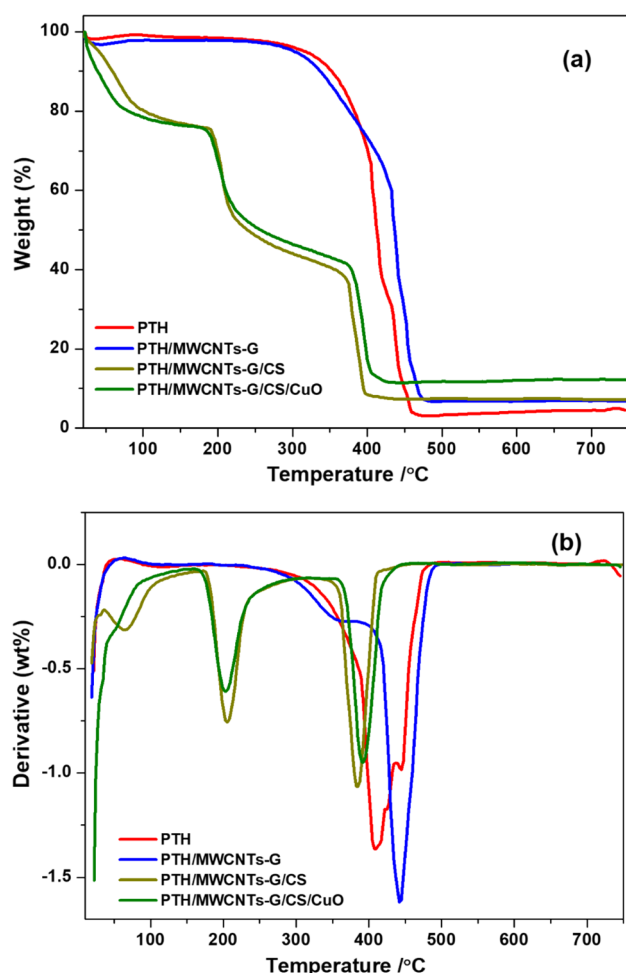Fig. 6 The TGA (**a**) and DTG (**b**) of modified polymers

$$i_p = 2.69 \times 10^5 An^{3/2}D^{1/2}Cv^{\frac{1}{2}} \tag{1}$$

where C is the concentration of $[Fe(CN)_6]^{3-/4-}$, i_p is the current, v is the scan rate, and A is the electrochemical surface area (cm^2) (n = 1, D = 7.6×10^{-5} cm^2 s^{-1}). Consequently, the electrode area for bare GCE and PTH/MWCNTs-G/CS/CuO/GCE was 0.034cm^2 and 0.0542 cm^2, respectively.

Hence, it is clear that PTH/MWCNTs-G/CS/CuO/GCE had the highest surface area (Figure S2).

To examine the electrolyte/electrode interfacial resistance, EIS measurements were carried out on bare GCE, PTH/GCE, PTH/MWCNTs-G/GCE, PTH/MWCNTs-G/CS/GCE, and PTH/ MWCNTs-G/CS/CuO/GCE (Fig. 8). The potential was set at 0.235 V against RE, with frequency ranging from 1 Hz to 100 kHz. A semi-circular portion at higher frequencies represents the charge transfer process, while the linear portion at lower frequencies is related to the diffusion process [52, 53]. Both bare and other modified electrodes exhibited the semi-circular portion followed by a diffusion tail, which is characteristic of the diffusion process and the best fit was with circuit description code R$_s$ (CPE(RctW)) (Fig. 8 inset), where R$_s$ is solution resistance, CPE is constant phase element, R$_{ct}$ is the charge transfer resistance, and W is the Warburg impedance. R$_{ct}$ values of 5900, 5700, 1409, 920, and 303 Ω cm^2 were recorded for GCE, PTH/GCE, PTH/MWCNTs-G/GCE, PTH/MWCNTs-G/CS/GCE, and PTH/ MWCNTs-G/CS/CuO/GCE, respectively. Furthermore, the plot of PTH/MWCNTs-G/Cs/CuO/GCE exhibited the smallest diameter semicircles, which suggests that conductivity was increased and the redox of $[Fe(CN)_6]^{3-/4-}$ was improved. Thus, we found that a combination of MWCNTs-G/CuO with polythiophene and decoration with chitosan led to high conductivity of fast electron between the nanocomposite (MWCNTs-G/CS/CuO) and underlying GCE surface.

3.3 Evaluation of the Electrocatalytic Activities of the Modified Electrode

The electrocatalytic activities of the oxidation of Cd(II) in aqueous solution were detected via CV based on the surface and conductivity. The voltammetric waves of bare GCE and PTH/MWCNTs-G/CS/CuO/GCE were measured in 70 μM and 0.1 M acetate buffer solution (AcB) at pH 4.5 (Fig. 9). No peak can be observed in Fig. 9b due to the absence of supporting redox probes. However, upon the addition of 70 μM of Cd(II) solution, anodic oxidation peaks of both electrodes can be observed (Fig. 9a, c). When compared with the current

Table 1 Thermal behavior of different modified polymers

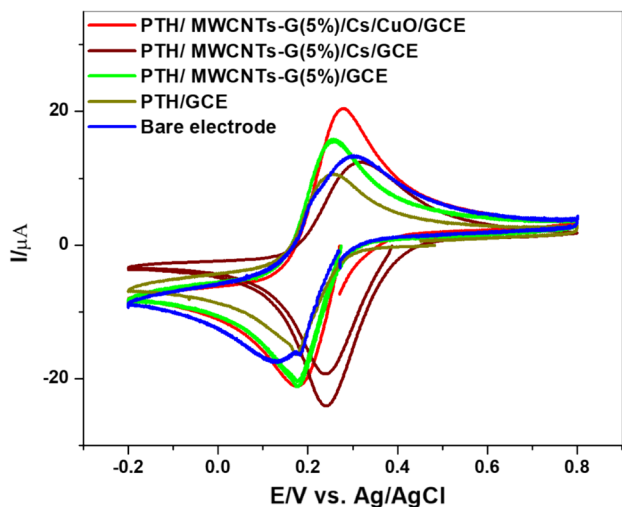| Sample	Temperature (°C)			PDT$_{max}$ (°C)	CDT$_{final}$ (°C)
	T$_{10}$	T$_{25}$	T$_{50}$		
PTH	364	406	418	430	480
PTH/ MWCNTs-G	347	416	443	450	500
PTH/ MWCNTs-G/CS	60	190	243	380	430
PTH/ MWCNTs-G/CS/CuO	36	189	254	400	446

Fig. 7 CVs of GCE and different loading GCE electrodes measured in 2 mM [Fe(CN)6]$^{3-/4-}$ and 0.1 M KCl
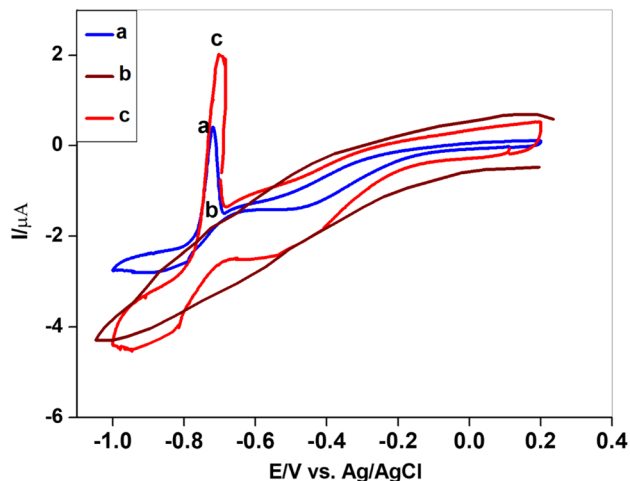

Fig. 9 CVs of (a) unmodified GCE c PTH/ MWCNTs-G/CS/CuO/ GCE upon addition 70 μM Cd(II) (0.1 M AcB, pH 4.5) at 0.05 V s-1. (b) PTH/ MWCNTs-G/CS/CuO/GCE in the absence of Cd(II)
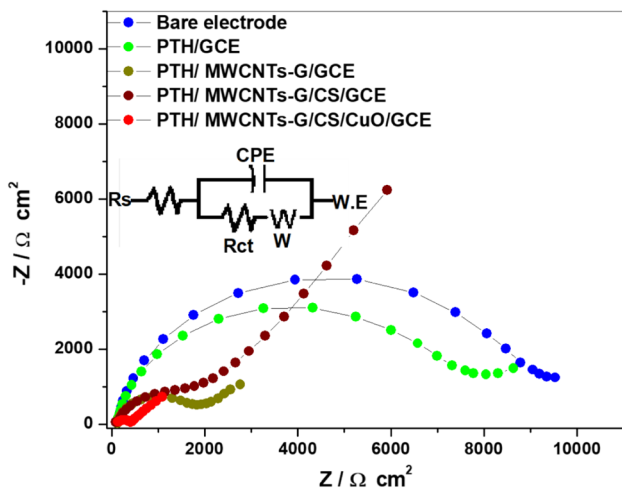

Fig. 8 Cole–Cole plots of bare electrode and different loading GCE measured in 2 mM [Fe(CN)$_6$]$^{3-/4-}$ and 0.1 M KCl
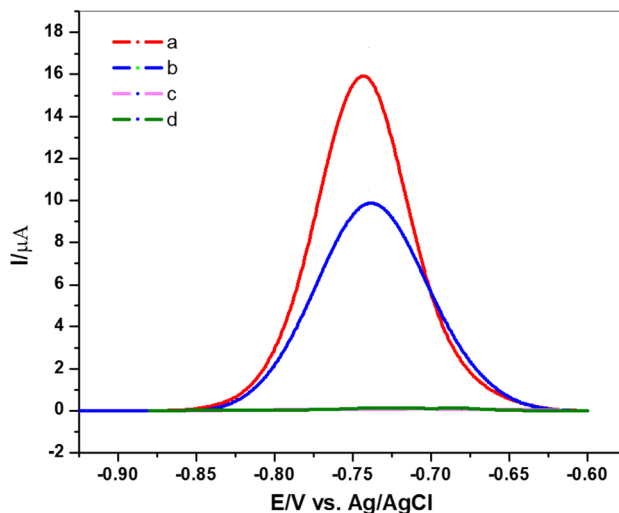

Fig. 10 SWV of (a) PTH/MWCNTs-G/CS/CuO/GCE; (b) unmodified GCE upon addition of 10 μM Cd(II) (0.1 M AcB, pH 4.5); (c) PTH/ MWCNTs-G/CS/CuO/GCE; and d unmodified GCE in the absence of Cd(II)

signal from the bare electrode, a well-defined sharp anodic peak was observed for PTH/MWCNTs-G/CS/CuO/GCE.

In the accumulation step, during the electrocatalysis process, the target Cd^{2+} was adsorbed on the PTH/MWCNTs-G/CS/CuO/GCE according to Eq. 2:

$$Cd^{2+} + 2e^- \rightarrow Cd^0 \tag{2}$$

while at the sweep potential from − 1.0 to 0.2 V, the oxidation process for the adsorbed Cd^0 took place according to Eq. 3.

$$Cd^0 \rightarrow Cd^{2+} + 2e^- \tag{3}$$

Thus, suggesting the effect of MWCNTs-G/CS/CuO, which provides several interactions between Cd(II) and electrode surface in the accumulation step such as hydrogen, electrostatic, and π–π bonds, functional group (amine/hydroxyl) in chitosan, which give high accumulation efficiency for the adsorption of Cd(II) [1, 50, 54].

Figure 10 shows the SWV of bare GCE and PTH/ MWCNTs-G/CS/CuO/GCE in a solution containing 10 μM Cd(II) in 0.1 M AcB at pH 4.5. The bare electrode (Fig. 10c) and PTH/MWCNTs-G/CS/CuO/GCE (Fig. 10d) show that the SWV signal in AcB in the absence of Cd(II) resulted

in no oxidation peak. The SWV of 10 μM of Cd(II) at the bare electrode exhibited an oxidation peak at potential of –0.735 V (Fig. 10a). Figure 10b shows the SWV of PTH/MWCNTs-G/CS/CuO/GCE, in which the oxidation signals appear at higher currents with a slight negative shift potential (–0.751 V) compared with the bare electrode. The above observations can be explained by the following points: First, using chitosan helps to form a film polymer with high electrochemical stability [1]; and second, in the accumulation step, Cd(II) adsorption occurs on the amine/hydroxy group in chitosan [1]. The nanocomposite can reduce surface fouling and enhance the charge transfer reaction [55, 56], and its surface has reactive groups that enhance the electrocatalytic activity of the newly synthesized materials [57, 58]. CuO is a p-type semiconductor with the capability to enhance the charge transfer reaction in electrochemical sensors application [59–61]. These findings suggest that the modification of the electrode with MWCNT-G, CuO, CS, and PTH enhanced the sensitivity and reduced the overpotential.

3.4 Optimization of Experimental Conditions for Determination of Cd(II)

3.4.1 Supporting Electrolyte Type and pH

We used SWV to study the effects of supporting electrolyte type and pH on the sensor's response to a solution of 10 μM Cd(II) with different buffer solutions including acetate buffer (AcB), Britton–Robinson buffer (BRB), and phosphate buffer solution (PBS) (each 0.01 M and pH 4.5), and the analysis results are shown in Fig. 11. It
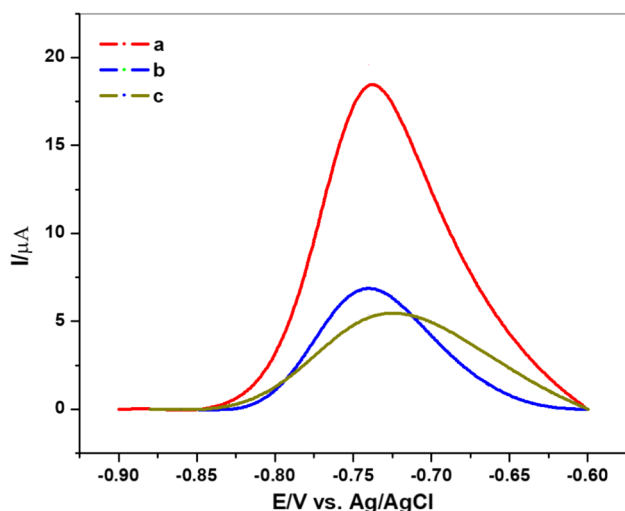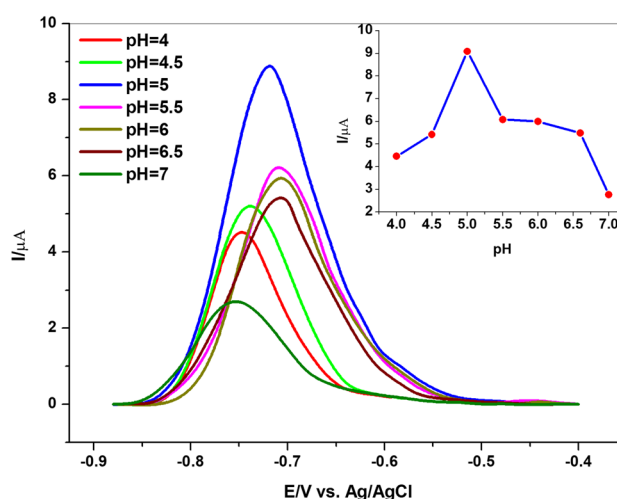

Fig. 12 The effect of pH on the SWV of the PTH/MWCNTs-G/CS/CuO/GCE in a solution containing 10 μM Cd(II). Inset: Plot of the current vs. pH

can be noted that response of Cd(II) had a very high current in 0.01 M AcB. Figure 12 depicts the SWV of 10 μM Cd(II) in 0.1 M AcB with pH varying from 4.0 to 7.0. The peak current initially increased from 4.0 to 5.0 and then decreased as the pH increased from 5.0 to 7.0 (Fig. 12 inset). This may have been caused by the hydrolysis of cadmium ions in neutral media [11]. Thus, the 0.1 M AcB at pH 5.0 was chosen as the optimum condition and was utilized in further experiments.

Fig. 11 The effect of (a) acetate buffer (AcB), (b) phosphate buffer solution (PBS), and (c) Britton-Robinson buffer (BRB) solution on the SWV of the PTH/ MWCNTs-G/CS/CuO/GCE in a solution containing 10 μM Cd(II)
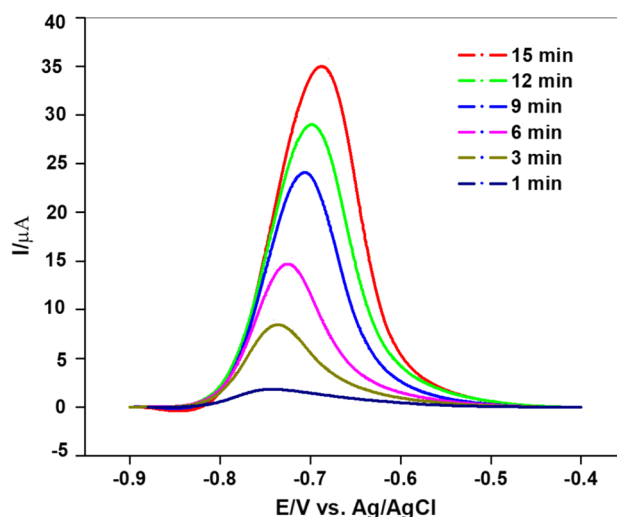

Fig. 13 Effect of accumulation time on the SWV of PTH/MWCNTs-G/CS/CuO/GCE in a solution containing 10 μM Cd(II) in 0.1 M AcB at pH 5.0 from –0.9 to –0.6 V

3.4.2 Effect of Accumulation Time

Accumulation time is an important parameter that can influence the sensitivity of detection of Cd(II). Figure 13 shows the peak current of Cd(II) with accumulation time ranging from 1 to 15 min. The peak current increased with accumulation time until reaching 15 min. This result may have been because the adsorption of cadmium on the surface of PTH/MWCNTs-G/CS/CuO/GCE attained a saturation level [7]. Hence, 15 min was selected as the optimum accumulation time in this work.

3.4.3 Effect of Scan Rate

To understand the electrochemical mechanism for the oxidation of Cd(II) at the surface of the modified electrode, cyclic voltammograms of 70 µM Cd(II) on PTH/MWCNTs-G/CS/CuO/GCE at different scan rates were recorded in 0.1 M AcB at pH 5.0 (Fig. 14). As shown in Fig. 14a, the peak potential shifted positively and the oxidation current increased as the scan rate increased from 1 to 150 mV s^{-1}, indicating that Cd(II) oxidation is an irreversible process [62]. The oxidation peak currents were linear with the square roots of the scan rate over the range

of 1 mV s^{-1} to 150 mV s^{-1} (Fig. 14b), indicating that diffusion plays an essential role in the oxidation process [63, 64]. The plot of log oxidation currents vs. log scan rate, i.e., $(\mu A) = -0.43 + 0.424 \log v \, (mVs^{-1})$, shown in Fig. 14c revealed a slope of 0.424 mV, providing further evidence that the reaction is a diffusion-controlled process.

3.5 The Electrochemical Sensing of Analyte at PTH/MWCNTs-G/CS/CuO/GCE

To investigate the catalytic activities of the modified electrode, the SWV of PTH/MWCNTs-G/CS/CuO/GCE over a series of concentrations of Cd(II) was studied under optimized conditions (Fig. 15a). The response current increased along with the Cd(II) concentration over a linear range between 0.01 and 30 µM. The regression equation is $i/\mu M = 2.59 \, C/\mu M + 1.191$ ($R^2 = 0.991$) (Fig. 15b). The LOD and LOQ were calculated as LOD = 3SD/s, and LOQ = 10SD/s, respectively [65], where SD is the standard deviation from 10 blank samples and s is the slope of the calibration plot (sensitivity). Due to the excellent catalytic activity of the nanocomposites, this procedure showed a high sensitivity of 2.59 µA µM^{-1}, with a detection limit of 0.014 µM and LOQ of 0.046 µM. A comparison of the
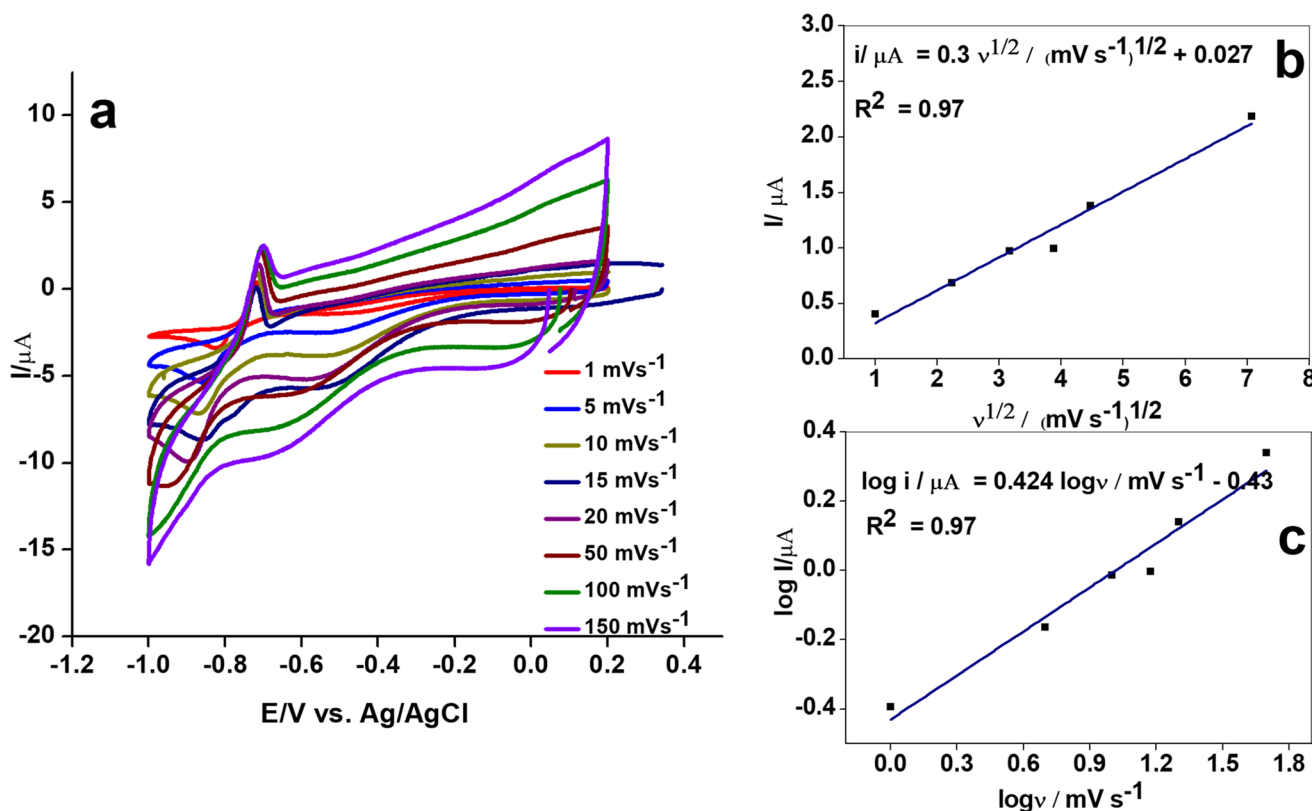

Fig. 14 **a** Effect of the scan rate on the CV of the PTH/ MWCNTs-G/CS/CuO/GCE in solution containing 70 µM Cd(II). **b** calibration plot of peak current vs. square root of scan rates, **c** plot of log peak current vs. log scan rates
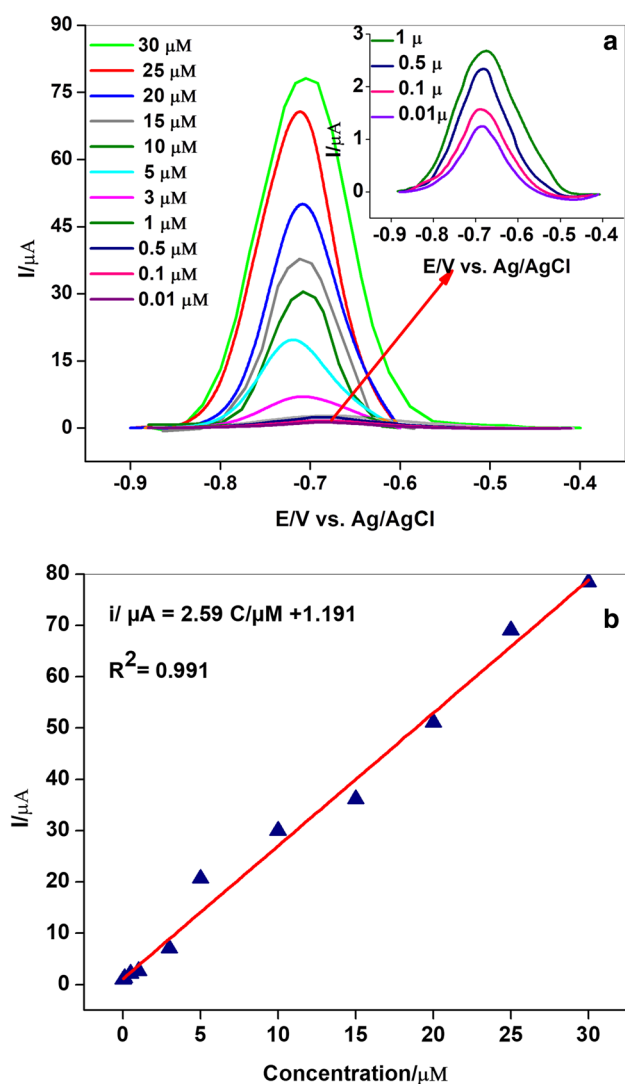
Fig. 15 **a** SWV response of the PTH/MWCNTs-G/CS/CuO/GCE for the analysis of Cd(II) over a concentration range of 0.01–30 μM in 0.1 M AcB at pH 5.0 from –0.9 to –0.6 V, and **b** corresponding linear calibration plot

electrodes' performance in terms of the detection of Cd(II) is shown in Table 2.

3.6 Reproducibility and Stability

A reproducible response in Cd(II) detection is an important property for electrochemical sensors. Thus, the operational reproducibility of the fabricated electrode was studied by measuring the SWV of 10 μM Cd(II) in 0.1 M AcB (pH 5.0) at a scan rate of 0.05 Vs^{-1} five times a day for 3 days (total of 15 measurements). The current response did not exhibit a remarkable decrease over this time and the relative standard deviation (RSD) value of reproducibility was found to be 8.05% (Figure S3). To analyze the stability of the Cd(II) response at PTH/MWCNTs-G/CS/CuO/GCE, the Cd(II) 10 μM concentration was investigated with the modified electrode under optimal conditions six times a day. The RSD of the peak was 5.2% (Figure S4), showing that there was satisfactory stability of the current peak for PTH/ MWCNTs-G/CS/CuO/GCE.

3.7 Interference Study

To estimate the interference, the SWV response of the PTH/ MWCNTs-G/CS/CuO/GCE toward Cd(II) and other interfering species, such as Na^+, Fe(III), and Cu(II), was studied. The responses of 10 μM Cd(II) and different concentrations of Na^+ (5, 10, 15, 20, and 30 μM) are shown in Figure S5. The tolerance limit was considered as the threshold limit concentration of the coexisting ions, which can cause a deviation in the original current response of more than 10% RSD [70]. According to the change in current response, coexisting ions exhibited little change in the original current response, while where at 30 times higher concentration of Na^+ the RSD was 8.643%. The same procedure was carried out under different concentrations of Fe(III), with an RSD of 8.682% at 30 times the baseline Fe(III) concentration. These results indicate that the PTH/ MWCNTs-G/CS/CuO/GCE had good selectivity for Cd(II). As predicted, the presence of Cu(II) during Cd(II) detection leads to a reduced current signal,

Table 2 Comparison of the modified electrode for the detection of Cd(II)

Electrode	Method	Linear range (μM)	LOD (μM)	Refs.
M-ɤ -Al$_2$O$_3$/CPE	DPV	0.01–10	0.002	[7]
Fe$_3$O$_4$/F-MWCNTs/GCE	SWV	0.048–30	0.014	[9]
SNAC/GCE	DPV	0.09–4.8	0.024	[66]
Alk-Ti$_3$C$_2$/GCE	SWV	0.1–1.5	0.098	[67]
BiF$_4$/CPE	ASV	0.18–0.89	0.087	[68]
Hg–Bi/SWCNT/GCE	SWV	0.089–1.2	0.018	[69]
PTH/MWCNTs-G/CS/CuO/GCE	SWV	0.01–30	0.014	This work

SNAC spherical carbon nanoparticle, *Alk-Ti₃C₂* alkalization-intercalated Ti3C2, *ASV* anodic stripping voltammetric, *SWCNT* single-walled carbon nanotubes

Table 3 Determination of Cd(II) in tap water samples

Sample	Amount added (μM)	Amount found (μM)	Recovery (%)
1	0	0	–
2	25	26.0	104.0
3	20	20.57	102.8
4	15	13.83	92.23
5	5	5.52	110.4

due to the generation of intermetallic compounds which can compete with Cd(II) and minimize the effective surface area of the electrode. This interference is quite similar to that reported by other researches [1, 7, 11, 71].

3.8 Analysis of Real Samples and Recovery Test

Tap water was used to study the practical application of PTH/MWCNTs-G/CS/CuO/GCE to determine Cd(II), and this was analyzed using a recovery procedure (Figure S6). A known concentration of Cd(II) (0, 5, 15, 20, and 25 μM) was added to 1.0 ml of the real sample, and the resulting solution was utilized to detect the recovery using Eq. 4 [65].

$$Recovery = \frac{C_{found}}{C_{added}} \times 100 \tag{4}$$

As shown in Table 3, the SWV of tap water sample did not show any response signal in absence of an analyte and the results of the Cd(II) in the real samples were between 92.23 and 110.4%. The results achieved from this analysis are considered quite reasonable.

4 Conclusions

A series of nanocomposites were prepared using an achievable in situ polymer oxidation route. A GCE modified electrode was applied for the detection of Cd(II) in 0.1 M AcB. The PTH/MWCNTs-G/CS/CuO sensor showed the best performance at a pH of 5.0. The LOD was found to be 0.014 μM and had an LOQ of 0.049 μM. The stability, reproducibility, and selectivity were evaluated and found to be sufficiently good. Furthermore, the fabricated electrode exhibited high performance with a real sample. The high Cd(II) detection efficiency of the PTH/MWCNTs-G/CS/CuO/GCE sensor indicated that it may be a successful candidate for electrochemical sensor applications.

Declarations

References

1. P. Sengupta, K. Pramanik, P. Sarkar, Simultaneous detection of trace Pb (II), Cd (II) and Hg (II) by anodic stripping analyses with glassy carbon electrode modified by solid phase synthesized iron-aluminate nano particles. Sens. Actuators B Chem. **329**, 129052 (2020)
2. M.-L. Lin, S.-J. Jiang, Determination of As, Cd, Hg and Pb in herbs using slurry sampling electrothermal vaporisation inductively coupled plasma mass spectrometry. Food Chem. **141**(3), 2158–2162 (2013)
3. M.S. Jiménez, M.T. Gómez, J.R. Castillo, Multi-element analysis of compost by laser ablation-inductively coupled plasma mass spectrometry. Talanta **72**(3), 1141–1148 (2007)
4. Q. Zhou, M. Lei, Y. Liu, Y. Wu, Y. Yuan, Simultaneous determination of cadmium, lead and mercury ions at trace level by magnetic solid phase extraction with Fe@ Ag@ Dimercaptobenzene coupled to high performance liquid chromatography. Talanta **175**, 194–199 (2017)
5. M. Thirumalai, S.N. Kumar, D. Prabhakaran, N. Sivaraman, M.A. Maheswari, Dynamically modified C18 silica monolithic column for the rapid determinations of lead, cadmium and mercury ions by reversed-phase high-performance liquid chromatography. J. Chromatogr. A **1569**, 62–69 (2018)
6. S. Li et al., Electrochemical microfluidics techniques for heavy metal ion detection. Analyst **143**(18), 4230–4246 (2018)
7. X. Zheng et al., Highly sensitive determination of lead (ii) and cadmium (ii) by a large surface area mesoporous alumina modified carbon paste electrode. Rsc Adv. **8**(14), 7883–7891 (2018)
8. C. Göde, M.L. Yola, A. Yılmaz, N. Atar, S. Wang, A novel electrochemical sensor based on calixarene functionalized reduced graphene oxide: application to simultaneous determination of Fe (III), Cd (II) and Pb (II) ions. J. Colloid Interface Sci. **508**, 525–531 (2017)
9. W. Wu et al., Simultaneous voltammetric determination of cadmium (II), lead (II), mercury (II), zinc (II), and copper (II) using a glassy carbon electrode modified with magnetite (Fe3O4) nanoparticles and fluorinated multiwalled carbon nanotubes. Microchim. Acta **186**(2), 1–10 (2019)
10. A. Moutcine et al., Preparation, characterization and simultaneous electrochemical detection toward Cd (II) and Hg (II) of a phosphate/zinc oxide modified carbon paste electrode. Inorg. Chem. Commun. **116**, 107911 (2020)
11. H. Dai, N. Wang, D. Wang, H. Ma, M. Lin, An electrochemical sensor based on phytic acid functionalized polypyrrole/graphene oxide nanocomposites for simultaneous determination of Cd (II) and Pb (II). Chem. Eng. J. **299**, 150–155 (2016)
12. Y. Liu, J. Tang, X. Chen, J.H. Xin, Decoration of carbon nanotubes with chitosan. Carbon N. Y. **43**(15), 3178–3180 (2005)
13. C.K.S. Pillai, W. Paul, C.P. Sharma, Chitin and chitosan polymers: chemistry, solubility and fiber formation. Prog. Polym. Sci. **34**(7), 641–678 (2009)

14. I. Younes, M. Rinaudo, Chitin and chitosan preparation from marine sources. Structure, properties and applications. Mar. Drugs **13**(3), 1133–1174 (2015)

15. S.D. Guna Vathana, J. Wilson, R. Prashanthi, A.C. Peter, CuO nanoflakes anchored Polythiophene nanocomposite: voltammetric detection of L-Tryptophan. Inorg. Chem. Commun. **124**, 108398 (2020)

16. S.A. Alqarni, M.A. Hussein, A.A. Ganash, Highly sensitive and selective electrochemical determination of sunset yellow in food products based on AuNPs/PANI-co-PoAN-co-PoT/GO/Au electrode. ChemistrySelect **3**(46), 13167–13177 (2018). https://doi.org/10.1002/slct.201802528

17. M.A. Hussein, A.A. Ganash, S.A. Alqarni, Electrochemical sensor-based gold nanoparticle/poly(aniline-co-o-toluidine)/graphene oxide nanocomposite modified electrode for hexavalent chromium detection: a real test sample. Polym. Technol. Mater. **58**(13), 1423–1436 (2019). https://doi.org/10.1080/25740881.2018.1563121

18. D.F. Katowah et al., Selective Hg2+ sensor performance based various carbon-nanofillers into CuO-PMMA nanocomposites. Polym. Adv. Technol. **31**(9), 1946–1962 (2020)

19. D.F. Katowah, M.A. Hussein, M.M. Rahman, Q.A. Alsulami, M.M. Alam, A.M. Asiri, Fabrication of hybrid PVA-PVC/SnZnOx/SWCNTs nanocomposites as Sn^{2+} ionic probe for environmental safety. Polym. Technol. Mater. **59**(6), 642–657 (2020)

20. D.F. Katowah et al., Selective fabrication of an electrochemical sensor for Pb^{2+} based on Poly (pyrrole-co-o–toluidine)/$CoFe_2O_4$ Nanocomposites. ChemistrySelect **4**(35), 10609–10619 (2019)

21. D.F. Katowah et al., The performance of various SWCNT loading into CuO–PMMA nanocomposites towards the detection of Mn 2+ ions. J. Inorg. Organomet. Polym. Mater. **30**, 5024–5041 (2020)

22. D.F. Katowah et al., Designed network of ternary core-shell PPCOT/NiFe2O4/C-SWCNTs nanocomposites. A Selective Fe^{3+} ionic sensor. J. Alloys Compd **834**, 155020 (2020)

23. K. Rovina, S. Siddiquee, S. Md Shaarani, An electrochemical sensor for the determination of tartrazine based on CHIT/GO/MWCNTs/AuNPs composite film modified glassy carbon electrode. Drug Chem. Toxicol **44**, 447 (2019)

24. A. Husain, S. Ahmad, F. Mohammad, Synthesis, characterisation and ethanol sensing application of polythiophene/graphene nanocomposite. Mater. Chem. Phys. (2020). https://doi.org/10.1016/j.matchemphys.2019.122324

25. A. Husain, S. Ahmad, F. Mohammad, Electrical conductivity and alcohol sensing studies on polythiophene/tin oxide nanocomposites. J. Sci. Adv. Mater. Devices **5**(1), 84–94 (2020). https://doi.org/10.1016/j.jsamd.2020.01.002

26. D.F. Katowah et al., Ternary nanocomposite based poly(pyrrole-co-O-toluidine), cobalt ferrite and decorated chitosan as a selective Co2+ cationic sensor. Compos. Part B-Eng. (2019). https://doi.org/10.1016/j.compositesb.2019.107175

27. B. Senthilkumar, P. Thenamirtham, R.K. Selvan, Structural and electrochemical properties of polythiophene. Appl. Surf. Sci. **257**(21), 9063–9067 (2011)

28. J. Mårdalen, E.J. Samuelsen, O.R. Gautun, P.H. Carlsen, X-ray scattering from oriented poly (3-alkylthiophenes). Synth. Met. **48**(3), 363–380 (1992)

29. Y. Li, G. Vamvounis, S. Holdcroft, Tuning optical properties and enhancing solid-state emission of poly (thiophene) s by molecular control: a postfunctionalization approach. Macromolecules **35**(18), 6900–6906 (2002)

30. T.S. Swathy, M.J. Antony, Tangled silver nanoparticles embedded polythiophene-functionalized multiwalled carbon nanotube nanocomposites with remarkable electrical and thermal properties". Polymer (Guildf) **189**, 122171 (2020)

31. M.E.I. Badawy, T.M.R. Lotfy, S.M.S. Shawir, Preparation and antibacterial activity of chitosan-silver nanoparticles for application in preservation of minced meat. Bull. Natl. Res. Cent. **43**(1), 1–14 (2019)

32. D. Thanasamy, D. Jesuraj, V. Avadhanam, A novel route to synthesis polythiophene with great yield and high electrical conductivity without post doping process. Polymer (Guildf) **175**, 32–40 (2019)

33. F.A. Harraz, M. Faisal, M. Jalalah, A.A. Almadiy, S.A. Al-Sayari, M.S. Al-Assiri, Conducting polythiophene/alpha-Fe2O3 nanocomposite for efficient methanol electrochemical sensor. Appl. Surf. Sci. (2020). https://doi.org/10.1016/j.apsusc.2019.145226

34. Y. Xie et al., Preparation and electromagnetic properties of chitosan-decorated ferrite-filled multi-walled carbon nanotubes/polythiophene composites. Compos. Sci. Technol. **99**, 141–146 (2014)

35. S.D. GunaVathana, P. Thivya, J. Wilson, A.C. Peter, Sensitive voltammetric sensor based on silver dendrites decorated polythiophene nanocomposite: Selective determination of L-Tryptophan. J. Mol. Struct. (2020). https://doi.org/10.1016/j.molstruc.2019.127649

36. F. Avilés, J.V. Cauich-Rodríguez, L. Moo-Tah, A. May-Pat, R. Vargas-Coronado, Evaluation of mild acid oxidation treatments for MWCNT functionalization. Carbon N. Y. **47**(13), 2970–2975 (2009)

37. C.L. Poh, M. Mariatti, A.F.M. Noor, O. Sidek, T.P. Chuah, S.C. Chow, Dielectric properties of surface treated multi-walled carbon nanotube/epoxy thin film composites. Compos. Part B Eng. **85**, 50–58 (2016)

38. M. Senel et al., Enhanced electrochemical sensing performance by in situ electrocopolymerization of pyrrole and thiophene-grafted chitosan. Int. J. Biol. Macromol. **143**, 582–593 (2020). https://doi.org/10.1016/j.ijbiomac.2019.12.013

39. H. Vijeth, S.P. Ashokkumar, L. Yesappa, M. Vandana, H. Devendrappa, Camphor sulfonic acid surfactant assisted polythiophene nanocomposite for efficient electrochemical hydrazine sensor. Mater. Res. Express (2019). https://doi.org/10.1088/2053-1591/ab5ef5

40. T. Ramachandran, V.V. Dhayabaran, Utilization of a MnO2/polythiophene/rGO nanocomposite modified glassy carbon electrode as an electrochemical sensor for methyl parathion. J. Mater. Sci. Electron. **30**(13), 12315–12327 (2019). https://doi.org/10.1007/s10854-019-01590-9

41. J. Zhao et al., Preparation and characterization of an electromagnetic material: the graphene nanosheet/polythiophene composite. Synth. Met. **181**, 110–116 (2013)

42. B.X. Valderrama-García, E. Rodríguez-Alba, E.G. Morales-Espinoza, K. Moineau Chane-Ching, E. Rivera, Synthesis and characterization of novel polythiophenes containing pyrene chromophores: thermal, optical and electrochemical properties. Molecules **21**(2), 172 (2016)

43. A.K. Thakur, M. Majumder, R.B. Choudhary, S.N. Pimpalkar, Supercapacitor based on electropolymerized polythiophene and multiwalled carbon nanotubes composites. IOP Conf. Ser.: Mater. Sci. Eng. **149**(1), 12166 (2016)

44. S. Khanmohammadi et al., Polythiophene/TiO_2 and polythiophene/ZrO2 nanocomposites: physical and antimicrobial properties against common infections. Biointerface Res. Appl. Chem. **8**(4), 3457–3462 (2018)

45. B. Singh, R.-A. Doong, D.S. Chauhan, A.K. Dubey, Synthesis and characterization of Fe_3O_4/Polythiophene hybrid nanocomposites for electroanalytical application". Mater. Chem. Phys. **205**, 462–469 (2018). https://doi.org/10.1016/j.matchemphys.2017.11.040

46. M.A. Hussein, B.M. Abu-Zied, A.M. Asiri, The role of mixed graphene/carbon nanotubes on the coating performance of G/

CNTs/epoxy resin nanocomposites. Int. J. Electrochem. Sci **11**, 7644–7659 (2016)

47. D.F. Katowah, G.I. Mohammed, D.A. Al-Eryani, O.I. Osman, T.R. Sobahi, M.A. Hussein, Fabrication of conductive cross-linked polyaniline/G-MWCNTS core-shell nanocomposite: a selective sensor for trace determination of chlorophenol in water samples. Polym. Adv. Technol. **31**(11), 2615–2631 (2020)

48. S. Parvez et al., Preparation and characterization of artificial skin using chitosan and gelatin composites for potential biomedical application. Polym. Bull. **69**(6), 715–731 (2012)

49. G. Ma, D. Yang, J.F. Kennedy, J. Nie, Synthesize and characterization of organic-soluble acylated chitosan. Carbohydr. Polym. **75**(3), 390–394 (2009)

50. A.H. Gedam, R.S. Dongre, Adsorption characterization of Pb (II) ions onto iodate doped chitosan composite: equilibrium and kinetic studies. RSC Adv. **5**(67), 54188–54201 (2015)

51. A. Bard, *Electrochemical Merhods. Fundamentals and Applications*, vol. 290 (Wiley, New York, 1980)

52. R. Madhuvilakku, S. Alagar, R. Mariappan, S. Piraman, Glassy carbon electrodes modified with reduced graphene oxide-MoS2-poly (3, 4-ethylene dioxythiophene) nanocomposites for the non-enzymatic detection of nitrite in water and milk. Anal. Chim. Acta **1093**, 93–105 (2020). https://doi.org/10.1016/j.aca.2019.09.043

53. R. Pauliukaite, M.E. Ghica, O. Fatibello-Filho, C.M.A. Brett, Electrochemical impedance studies of chitosan-modified electrodes for application in electrochemical sensors and biosensors. Electrochim. Acta **55**(21), 6239–6247 (2010). https://doi.org/10.1016/j.electacta.2009.09.055

54. S. Sakthinathan et al., Platinum incorporated mordenite zeolite modified glassy carbon electrode used for selective electrochemical detection of mercury ions. Microporous Mesoporous Mater. **292**, 109770 (2020)

55. A.J. Ahammad, J.-J. Lee, M. Rahman, Electrochemical sensors based on carbon nanotubes. Sensors **9**(4), 289–2319 (2009)

56. S. Lü, Electrochemical determination of 8-azaguanine in human urine at a multi-carbon nanotubes modified electrode. Microchem. J. **77**(1), 37–42 (2004)

57. C. Hu, S. Hu, Carbon nanotube-based electrochemical sensors: principles and applications in biomedical systems. J. Sens. (2009). https://doi.org/10.1155/2009/187615

58. G.A. Rivas et al., Carbon nanotubes for electrochemical biosensing. Talanta **74**(3), 291–307 (2007)

59. Z. Amirzadeh, S. Javadpour, M.H. Shariat, R. Knibbe, Non-enzymatic glucose sensor based on copper oxide and multi-wall carbon nanotubes using PEDOT: PSS matrix. Synth. Met. **245**, 160–166 (2018)

60. L. Hou et al., CO gas sensors based on p-type CuO nanotubes and CuO nanocubes: morphology and surface structure effects on the sensing performance. Talanta **188**, 41–49 (2018)

61. Q. Zhang et al., CuO nanostructures: synthesis, characterization, growth mechanisms, fundamental properties, and applications. Prog. Mater. Sci. **60**, 208–337 (2014)

62. J. Wu, W. Wang, M. Wang, H. Liu, H. Pan, Electrochemical behavior and direct quantitative determination of tanshinone IIA in micro-emulsion. Int. J. Electrochem. Sci. **11**(6), 5165–5179 (2016). https://doi.org/10.20964/2016.06.55

63. E. Laviron, L. Roullier, C. Degrand, A multilayer model for the study of space distributed redox modified electrodes: Part II. Theory and application of linear potential sweep voltammetry for a simple reaction. J. Electroanal. Chem. Interfacial Electrochem. **112**(1), 11–23 (1980)

64. N.M. Thanh, N.D. Luyen, T.T.T. Toan, N.H. Phong, N. Van Hop, Voltammetry determination of Pb(II), Cd(II), and Zn(II) at Bismuth Film electrode combined with 8-hydroxyquinoline as a complexing agent. J. Anal. Methods Chem. (2019). https://doi.org/10.1155/2019/4593135

65. E. Desimoni, B. Brunetti, Presenting analytical performances of electrochemical sensors. some suggestions. Electroanalysis **25**(7), 1645–1651 (2013). https://doi.org/10.1002/elan.201300150

66. R. Madhu, K.V. Sankar, S.-M. Chen, R.K. Selvan, Eco-friendly synthesis of activated carbon from dead mango leaves for the ultrahigh sensitive detection of toxic heavy metal ions and energy storage applications. Rsc Adv. **4**(3), 1225–1233 (2014)

67. X. Zhu et al., Alkaline intercalation of Ti3C2 MXene for simultaneous electrochemical detection of Cd (II), Pb (II), Cu (II) and Hg (II). Electrochim. Acta **248**, 46–57 (2017)

68. H. Sopha et al., A new type of bismuth electrode for electrochemical stripping analysis based on the ammonium tetrafluorobismuthate bulk-modified carbon paste. Electroanalysis **22**(13), 1489–1493 (2010)

69. R. Ouyang, Z. Zhu, C.E. Tatum, J.Q. Chambers, Z.-L. Xue, Simultaneous stripping detection of Zn (II), Cd (II) and Pb (II) using a bimetallic Hg–Bi/single-walled carbon nanotubes composite electrode. J. Electroanal. Chem. **656**(1–2), 78–84 (2011)

70. H. Lin, G. Li, K. Wu, Electrochemical determination of Sudan I using montmorillonite calcium modified carbon paste electrode. Food Chem. **107**(1), 531–536 (2008). https://doi.org/10.1016/j.foodchem.2007.08.022

71. C. Kokkinos, A. Economou, I. Raptis, C.E. Efstathiou, Lithographically fabricated disposable bismuth-film electrodes for the trace determination of Pb (II) and Cd (II) by anodic stripping voltammetry. Electrochim. Acta **53**(16), 5294–5299 (2008)